PAPER

Check for updates

Catalytically active ceria-supported cobalt–manganese oxide nanocatalysts for oxidation of carbon monoxide†

Xu Wang, [ab] Lin-Ying Du, [c] Meng Du, [ad] Chao Ma, *[e] Jie Zeng, [e] Chun-Jiang Jia [ID] *[c] and Rui Si [ID] *[a]

A low-concentration cobalt (~6 at%) and manganese (~3 at%) bimetallic oxide catalyst supported on ceria nanorods ($CoMnO_x/CeO_2$), as well as its related single metal oxide counterparts (CoO_x/CeO_2 and MnO_x/CeO_2) was synthesized *via* a deposition–precipitation approach. The fresh samples after air-calcination at 400 °C were tested under the reaction conditions of CO oxidation, and showed the following order of reactivity: $CoMnO_x/CeO_2 > CoO_x/CeO_2 > MnO_x/CeO_2$. X-ray diffraction (XRD) and transmission electron microscopy (TEM) data identified that the structure of the CeO_2 support was maintained during deposition of metal (Co, Mn) ions while the corresponding vis-Raman spectra verified that more oxygen vacancies were created after deposition–precipitation than those in pure ceria nanorods. Aberration-corrected, high-angle, annular dark-field scanning transmission electron microscopy (HAADF-STEM) images with the help of electron energy loss spectroscopy (EELS) analyses determined two types of cobalt species, *i.e.* ultra-fine clusters (<2 nm) and smaller nanocrystals (up to 5 nm) in CoO_x/CeO_2 while only bigger nanostructures (~10 nm) of cobalt–manganese oxides in $CoMnO_x/CeO_2$. X-ray absorption fine structure (XAFS) measurements demonstrated the presence of a cubic Co_3O_4 phase in all the cobalt-based catalysts. The fitting results of the extended X-ray absorption fine structure (EXAFS) indicated that the introduction of the secondary metal (Mn) oxide significantly enhanced the two-dimensional growth of cobalt oxide nanostructures on the surface of CeO_2. Therefore, the enhanced activity of CO oxidation reaction over the bimetallic cobalt–manganese oxide nanocatalyst can be attributed to the higher crystallinity of the Co_3O_4 phase in this work.

Introduction

Low-temperature CO oxidation over nanosized metal[1,2] or metal oxide[3–6] catalysts has been one of the most extensively studied systems in heterogeneous catalysis. Among them, nanostructured cobalt oxide (*e.g.* Co_3O_4) has attracted much research interest due to its remarkable activity under the extreme low-temperature conditions.[6–8] For instance, Xie *et al.* developed a hydrothermal method using cobalt hydroxide as a precursor and subsequent direct thermal decomposition to obtain Co_3O_4 nanorods with exposed {110} facets composed of plenty of active Co^{3+} species, which showed better catalytic properties than the Co_3O_4 nanoparticles for CO oxidation at temperatures as low as −77 °C.[6] Hu *et al.* subsequently confirmed that the Co_3O_4 nanobelts primarily enclosed by the {110} surface are more active than the Co_3O_4 nanocubes terminated by the {100} planes, indicating the importance of the exposed surface of cobalt oxide nanostructures for oxidation of carbon monoxide.[9] Although surface Co^{3+} ions have been proposed to be an active species for the CO oxidation reaction,[6,9,10] it is still very difficult to have a full understanding of the investigated "structure–activity" relationship in cobalt oxide nanostructures. Multiple factors, including the size of Co_3O_4,[8,11] the oxidation state of cobalt species,[12,13] the effect of various oxide supports,[14,15] the metal–support interaction,[16,17] and even the influence of impurities such as trace amounts of water[9,18,19] can significantly modify the catalytic performance of cobalt oxide nanocatalysts.

[a] *Shanghai Synchrotron Radiation Facility, Shanghai Institute of Applied Physics, Chinese Academy of Sciences, Shanghai 201204, China. E-mail: sirui@sinap.ac.cn*

[b] *University of Chinese Academy of Science, Beijing 10049, China*

[c] *Key Laboratory for Colloid and Interface Chemistry, Key Laboratory of Special Aggregated Materials, School of Chemistry and Chemical Engineering, Shandong University, Jinan 250100, China. E-mail: jiacj@sdu.edu.cn*

[d] *Department of Chemistry, College of Science, Shanghai University, Shanghai 200444, China*

[e] *Hefei National Laboratory for Physical Sciences at the Microscale, University of Science and Technology of China, Hefei, Anhui 230026, China. E-mail: cma@ustc.edu.cn*

† Electronic supplementary information (ESI) available: TEM and HRTEM images. See DOI: 10.1039/c7cp02004j

This journal is © the Owner Societies 2017

Phys. Chem. Chem. Phys., 2017, **19**, 14533–14542 | **14533**

Ceria-supported cobalt oxide catalyst is very active for CO oxidation and is also a typical research system for investigating the metal–support interaction.[16,17,20,21] For example, Luo et al. used a surfactant-templated method to prepare Co_3O_4–CeO_2 catalysts, which exhibited a volcano-type performance for CO oxidation with increased cobalt contents.[20] Deng et al. synthesized porous Co_3O_4–CeO_2 materials via decomposition of metal–organic complexes, and found that the 20 wt% Co sample displays the best reactivity on CO oxidation (50% conversion at 74 °C).[21] However, to date, very limited results on the effect of a secondary metal oxide on Co–Ce–O systems, i.e. bimetallic oxide nanocatalysts, have been reported.[22–24]

On the other hand, the precise and comprehensive detection of such complicated oxide supported metal or metal oxide nanocatalysts is extremely difficult in reality. Multiple advanced characterization techniques, including aberration-corrected, high-angle, annular, dark-field scanning transmission electron microscopy (HAADF-STEM) and X-ray absorption fine structure (XAFS), are required to complete these tasks.[25–29] Divins et al. carried out HAADF-STEM to identify the existence of bimetallic RhPd nanoparticles supported on the surface of ceria.[25] Kugai et al. conducted EXAFS analysis to reveal that Cu forms alloys with Pt and Pd on the surface of CeO_2.[26] Very recently, we combined the advantages of HAADF-STEM and XAFS characterization to demonstrate the active species of gold on ceria nanorods for the room-temperature CO oxidation reaction.[29] Nevertheless, the correlation between the technical data and the catalytic performance of these ceria-supported bimetallic oxide nanocatalysts should be very carefully examined to avoid any pseudo-phenomena or misleading conclusions.

In this work, we have used ceria nanorods as the oxide support, and simultaneously deposited cobalt and manganese ions via a deposition–precipitation synthesis method. With the aid of HAADF-STEM and XAFS techniques, we have systematically investigated the structural and textural properties of a bimetallic cobalt–manganese oxide nanocatalyst, comprehensively clarified the "structure–activity" relationship in a Co–Mn–Ce–O system by determining the active species of cobalt-based samples for the low-temperature CO oxidation reaction, and clearly uncovered that the introduction of a secondary metal (Mn) oxide significantly enhances the crystallinity of the active Co_3O_4 phase to promote the CO oxidation reactivity of bimetallic cobalt–manganese oxide nanocatalysts.

Results and discussion

The CO oxidation reaction ($2CO + O_2 = 2CO_2$) was used to evaluate the catalytic performance of ceria-supported cobalt–manganese oxide catalysts. The "light off" profiles in Fig. 1a under the transient mode display higher CO conversions on bimetallic oxide samples ($CoMnO_x$/CeO_2), compared to those on single metal oxide counterparts (CoO_x/CeO_2 and MnO_x/CeO_2). Table 1 shows that the temperature of 50% conversion (T_{50}) follows the sequence of $CoMnO_x$/CeO_2 (99 °C) < CoO_x/CeO_2 (122 °C) < MnO_x/CeO_2 (158 °C), corresponding to the order of
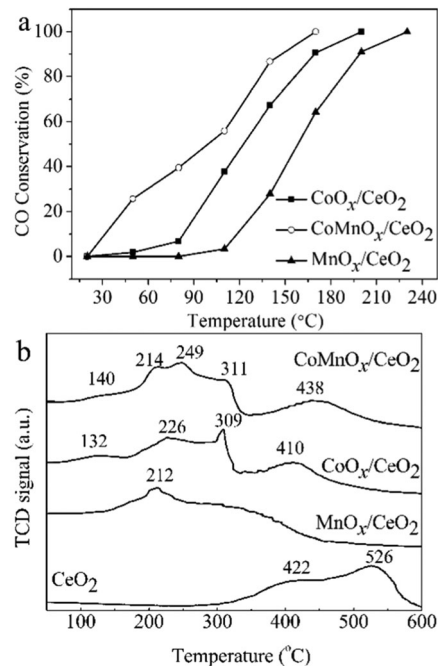
Fig. 1 (a) "Light off" for CO oxidation reaction (1%CO/20%O_2/N_2, 80 000 mL h^{-1} g$_{cat}$$^{-1}$) and (b) H_2-TPR profiles of ceria-supported cobalt–manganese oxide samples.

Table 1 Reduction temperatures (T_R), determined by H_2-TPR and 50% CO conversion (T_{50}), reaction rate (r) for cobalt and manganese at 80 °C in CO oxidation reaction for ceria-supported cobalt–manganese oxide clusters samples

Sample	T_R^{a} (°C)	T_{50}^{b} (°C)	r^b (μmol$_{CO}$ g$_{Co}$$^{-1}$ s^{-1})
CoO_x/CeO_2	132, 226, 309, 410	122	20
$CoMnO_x$/CeO_2	140, 214, 249, 311, 438	99	176
MnO_x/CeO_2	212	158	—

^{a} From H_2-TPR. ^{b} Tested in 1%CO/20%O_2/N_2 (80 000 mL h^{-1} g$_{cat}$$^{-1}$).

CO oxidation reactivity: $CoMnO_x$/CeO_2 > CoO_x/CeO_2 > MnO_x/CeO_2. We further calculated the reaction rates (r), normalized by the weight of Co metal, for the ceria-supported cobalt–manganese oxide samples. Table 1 shows that the r value of bimetallic oxides ($CoMnO_x$/CeO_2, 176 μmol$_{CO}$ g$_{Co}$$^{-1}$ s^{-1}) is over eight-fold that of the single metal oxide (CoO_x/CeO_2, 20 μmol$_{CO}$ g$_{Co}$$^{-1}$ s^{-1}) at 80 °C. These results indicate that the introduction of a secondary component (manganese oxide) to ceria-supported cobalt oxide catalyst can significantly improve its catalytic performance for the CO oxidation reaction.

Furthermore, Deng et al. prepared three-dimensional macro/mesoporous Co_3O_4–CeO_2 catalysts with T_{50} values for CO oxidation in the range of 50–175 °C under a lower space velocity of 30 000 mL h^{-1} g$_{cat}$$^{-1}$.[21] Luo et al. prepared Co_3O_4–CeO_2 nanocomposites with various Co/Ce ratios by a surfactant-templated method, and the most active catalyst exhibiting a T_{50} value of 94 °C for the CO oxidation reaction (10 000 mL h^{-1} g$_{cat}$$^{-1}$).[20] Mock et al. prepared 10 wt% Co–CeO_2 nanorods catalysts by the IMP method with T_{50} of 141 °C for CO oxidation (140 000 mL h^{-1} g$_{cat}$$^{-1}$).[30]

14534 | Phys. Chem. Chem. Phys., 2017, **19**, 14533–14542

This journal is © the Owner Societies 2017

Cwele *et al.* prepared $Ce_{0.90}Co_{0.10}O_{2-\delta}$ catalysts by the urea-assisted solution combustion method with T_{50} of 110 °C for CO oxidation (12 000 to 48 000 h^{-1}).[31] So, the reactivity of our ceria-supported cobalt–manganese oxide samples is comparable to the active Co–Ce–O catalysts in the literature.

In order to reveal the metal–support interaction between cobalt–manganese species and ceria nanorods, temperature programmed reduction by hydrogen (H$_2$-TPR) was applied over the fresh samples. Fig. 1b exhibits two broad bands at 422 °C and 526 °C for pure CeO$_2$ nanorods, which can be attributed to the surface reduction of CeO$_2$. However, only one single reduction peak at *ca.* 212 °C presents for MnO$_x$/CeO$_2$, which can be attributed to the surface reduction of CeO$_2$ correlating to the reduction of ionic Mn species.[32] Multiple steps can be identified for CoO$_x$/CeO$_2$, *i.e.* 132 °C by the reduction of the Co$_3$O$_4$ phase to CoO, 226 °C by the sequential reduction of as-formed CoO clusters to Co^0, 309 °C by the reduction of Co^{2+} ions interacting with CeO$_2$ and 410 °C by the reduction of surface Ce^{4+} ions from nanorods.[33] However, for the bimetallic cobalt–manganese oxide sample, the sum of these reduction peaks can be verified from Fig. 1b. Thus, according to these experimental data, both Co and Mn species strongly interact with the CeO$_2$ support, while no direct correlations between Co and Mn species were observed in our work.

Inductively coupled plasma atomic emission spectroscopy (ICP-AES) characterization was conducted to identify the concentrations of cobalt (C_{Co}) and manganese (C_{Mn}) in each sample after air-calcination at 400 °C. Table 2 shows that the determined C_{Co} (8.7 at%) and C_{Mn} (3.8 at%) numbers were close to the designed ones in CoO$_x$/CeO$_2$ (C_{Co} = 10 at%) and MnO$_x$/CeO$_2$ (C_{Mn} = 5 at%), respectively, showing the successful deposition–precipitation for the loading of single metal (Co or Mn) ions. For the ceria-supported bimetallic oxide catalyst (CoMnO$_x$/CeO$_2$), the values of C_{Co} (5.7 at%) and C_{Mn} (3.0 at%) were obviously lower than the theoretically calculated values (C_{Co} = 10 at% and C_{Mn} = 5 at%), indicating the partial loss of both cobalt and manganese species during the deposition–precipitation step. We noticed that the sum of C_{Co} and C_{Mn} in CoMnO$_x$/CeO$_2$ (8.7 at%) was identical to the pure C_{Co} number in CoO$_x$/CeO$_2$, suggesting that the saturated concentration of ∼10 at% for deposition of metal ions onto the surface of the CeO$_2$ support in our preparation. Recently, Gamboa-Rosales *et al.* prepared Au–Cu/ceria bimetallic catalysts by a similar deposition–precipitation route and found

that the maximum loading amount of highly dispersed copper species was ∼20 at%.[34]

Nitrogen adsorption experiments were carried out to investigate the textural properties of ceria-supported cobalt–manganese oxide samples. The BET specific surface areas of fresh samples air-calcined at 400 °C were 91–98 m^2 g^{-1}, well consistent with the previous report on doped ceria nanorods (80–97 m^2 g^{-1}),[35] which indicates that the deposition of various metal ions does not affect the surface area of the CeO$_2$ support in our work.

The X-ray diffraction (XRD) measurements were performed to determine the crystal structure of ceria-supported cobalt–manganese oxide catalysts. The XRD patterns in Fig. 2a show the fcc fluorite CeO$_2$ phase (JCPDS card no: 34-394) with lattice constants a of 5.4031–5.4086 Å (see Table 3) for all the fresh samples. The broadening of the diffraction lines indicates the nanocrystalline nature of the ceria nanorods. No peaks can be assigned to cobalt-containing (Co/CoO/Co$_2$O$_3$/Co$_3$O$_4$) or manganese-containing (Mn/MnO/Mn$_3$O$_4$/Mn$_2$O$_3$/MnO$_2$) phase in both CoMnO$_x$/CeO$_2$ and CoO$_x$/CeO$_2$ or MnO$_x$/CeO$_2$, revealing that the deposited cobalt and manganese species were either of very small grain sizes or highly dispersed clusters over the CeO$_2$ surface. Fig. 2b displays that the used samples maintained the same crystal structure as the fresh ones, which confirms the good stability of the ceria-supported cobalt–manganese oxide nanocatalysts during the CO oxidation process up to 200 °C in 1%CO/20%O$_2$/N$_2$. The a numbers of CoMnO$_x$/CeO$_2$ and CoO$_x$/CeO$_2$ or MnO$_x$/CeO$_2$ dropped to 5.3922–5.4018 Å after the reaction, probably due to the removal of surface hydroxyls under the working conditions.

Vis-Raman spectroscopy excited by a 532 nm laser was applied to finely determine the structure of ceria-supported
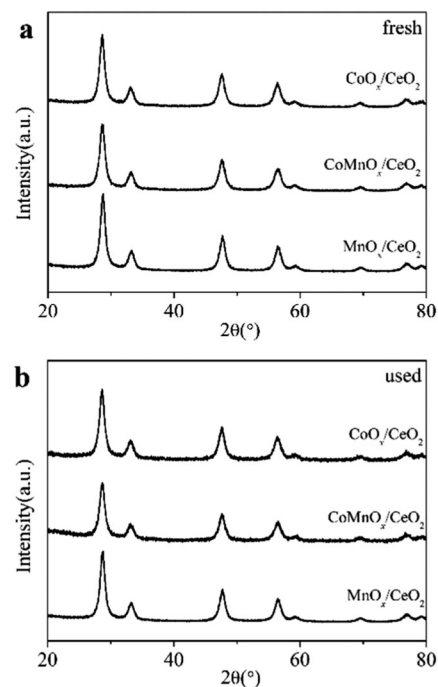
Fig. 2 XRD patterns of ceria-supported cobalt–manganese oxide samples: (a) fresh; (b) used.

Table 2 Metal concentrations of cobalt (C_{Co}) and manganese (C_{Mn}), surface metal ratio of Ce/Mn and surface component ratio of Mn^{2+}/Mn^{3+}/Mn^{4+} for ceria-supported cobalt–manganese oxide samples

Sample	C_{Co}^{a} (at%)	C_{Mn}^{a} (at%)	Mn/Ce^{b}	Mn^{2+}/Mn^{3+}/Mn^{4+b}
CoO$_x$/CeO$_2$	8.7	—	—	—
CoMnO$_x$/CeO$_2$	5.7	3.0	6.9/93.1	22/56/22
			7.3/92.7^c	22/54/24^c
MnO$_x$/CeO$_2$	—	3.8	8.5/91.5	21/58/21
			6.9/93.1^c	20/52/30^c

^{a} Determined by ICP-AES. ^{b} Determined by XPS. ^{c} For used samples after CO oxidation reaction.

This journal is © the Owner Societies 2017

Phys. Chem. Chem. Phys., 2017, **19**, 14533–14542 | **14535**

Paper

Table 3 The position (F_{2g}) and full width at half maximum (FWHM) of Raman spectra, lattice constants (a), averaged width size (D_w) and averaged grain size (D_g) of CeO_2 for ceria-supported cobalt–manganese oxide samples

Sample	F_{2g} (cm^{-1})	FWHM (cm^{-1})	a^a (Å)	$D_w{}^b$ (nm)	$D_g{}^c$ (nm)
CoO$_x$/CeO$_2$	445	64	5.4086	8.2 ± 1.6	7.7
	450^d	70^d	5.4018^d	8.0 ± 1.5^d	8.6^d
CoMnO$_x$/CeO$_2$	451	51	5.4043	8.0 ± 1.8	8.0
	445^d	71^d	5.3971^d	8.0 ± 1.6^d	8.0^d
MnO$_x$/CeO$_2$	451	76	5.4031	8.4 ± 1.6	9.5
	451^d	78^d	5.3922^d	8.2 ± 1.4^d	9.5^d

^{a} Calculated from the XRD patterns. ^{b} Calculated from more than 100 particles in TEM. ^{c} Estimated by Scherrer equation. ^{d} For used samples after CO oxidation reaction.
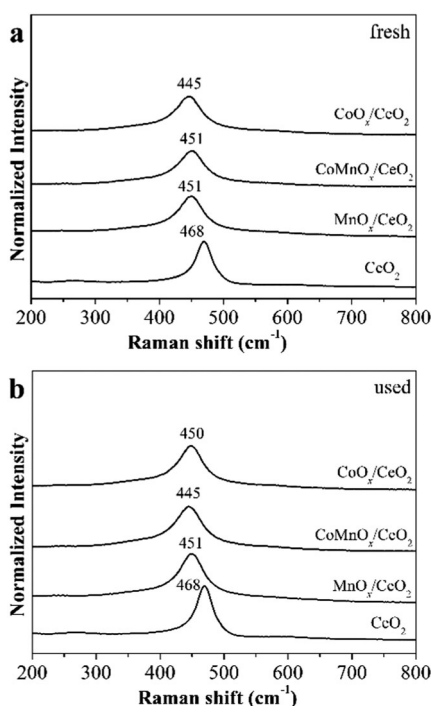
Fig. 3 Vis-Raman spectra of ceria-supported cobalt–manganese oxide samples: (a) fresh; (b) used.

cobalt–manganese oxide nanocatalysts. Fig. 3a distinctly exhibits a strong absorption centered at 445–451 cm^{-1}, corresponding to the triply degenerate F_{2g} mode of fluorite CeO_2.[36] Table 3 shows that the full width at half maximum (FWHM) of Raman spectra for ceria-supported cobalt–manganese varies from 51 to 76 cm^{-1}. This peak shifted to a lower wavelength and became broader, compared to that for pure ceria nanorods (position: 468 cm^{-1}; FWHM: 36 cm^{-1}). It suggests the presence of oxygen vacancies[37] for Co- and/or Mn-doped CeO_2, which were also deduced from the H_2-TPR results, i.e. activated oxygen species on surface of ceria nanorods. Fig. 3b exhibits that the Raman spectra of used samples (CoMnO$_x$/CeO$_2$ and CoO$_x$/CeO$_2$/MnO$_x$/CeO$_2$) were very similar to those of the fresh ones, revealing that

the defective structure (oxygen vacancies, etc.) was largely maintained for the ceria-supported cobalt–manganese oxide catalysts after the CO oxidation reaction.

Characterization using transmission electron microscopy (TEM) and high-resolution transmission electron microscopy (HRTEM) was done to determine the morphology, size and shape of ceria-supported cobalt–manganese oxide catalysts under a microdomain view. In particular, the TEM images in Fig. S1 (ESI†) show that both fresh and used samples, for both single metal oxide (CoO$_x$/CeO$_2$ or MnO$_x$/CeO$_2$) or bimetallic oxides (CoMnO$_x$/CeO$_2$), were composed of rod-like crystals with width (D_w) varying from 8.0 to 8.4 nm (see Table 3), close to that of pure CeO_2 nanorods (10.1 nm).[38] Fig. S2 (ESI†) also depicts the HRTEM images of a single nanorod, displaying the interplanar d-spacing for CeO_2 (111) or (200) planes. Similar to the related XRD results, no separate cobalt-containing (Co/CoO/Co$_2$O$_3$/Co$_3$O$_4$) or manganese-containing (Mn/MnO/Mn$_2$O$_3$/Mn$_3$O$_4$/MnO$_2$) nanoparticles can be identified in HRTEM.

Therefore, the obtained cobalt–manganese component was invisible in both XRD and TEM, and could consist of highly dispersed metal oxide species supported on the CeO_2 surface. Previously, Lin et al., synthesized a 7.1 wt% Co/CeO$_2$ catalyst via a coprecipitation method, which also displays no diffraction peaks or crystallized particles for the cobalt oxide phase.[39]

As discussed above, the XRD and TEM/HRTEM tests were unable to directly detect the nanostructure of active cobalt oxide species. Thus, we carried out the aberration-corrected HAADF-STEM with the help of EELS to obtain the spatial distribution of cobalt species in each sample at the atomic scale (resolution: ∼1 Å). Fig. 4 shows the HAADF-STEM images of CoO$_x$/CeO$_2$ and CoMnO$_x$/CeO$_2$, which is similar to the related TEM/HRTEM results. Furthermore, we observed a large number of surface voids for ceria nanorods, probably caused by the dehydration process during the growth of rod-like CeO_2 nanocrystals.[26]

Fig. 5 shows that Ce element was uniformly distributed over the field of view for both CoO$_x$/CeO$_2$ and CoMnO$_x$/CeO$_2$, due to the existence of a dominant CeO_2 skeleton. Fig. 5a exhibits that the Co-rich microdomains composed by either ultra-fine clusters of less than 2 nm or small aggregates of up to 5 nm were determined for CoO$_x$/CeO$_2$. However, for CoMnO$_x$/CeO$_2$, both Co-rich and Mn-rich nanostructures ∼10 nm in size appeared simultaneously (see Fig. 5b). It indicates that bimetallic
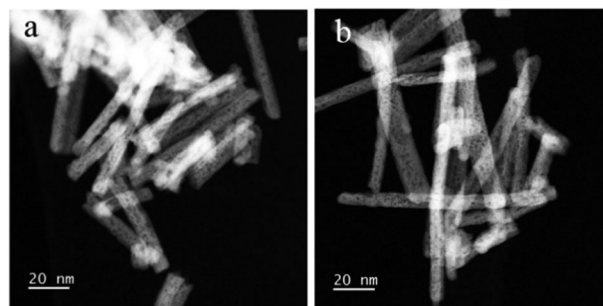
Fig. 4 HAADF-STEM images of ceria-supported cobalt–manganese oxide samples: (a) CoO$_x$/CeO$_2$; (b) CoMnO$_x$/CeO$_2$.
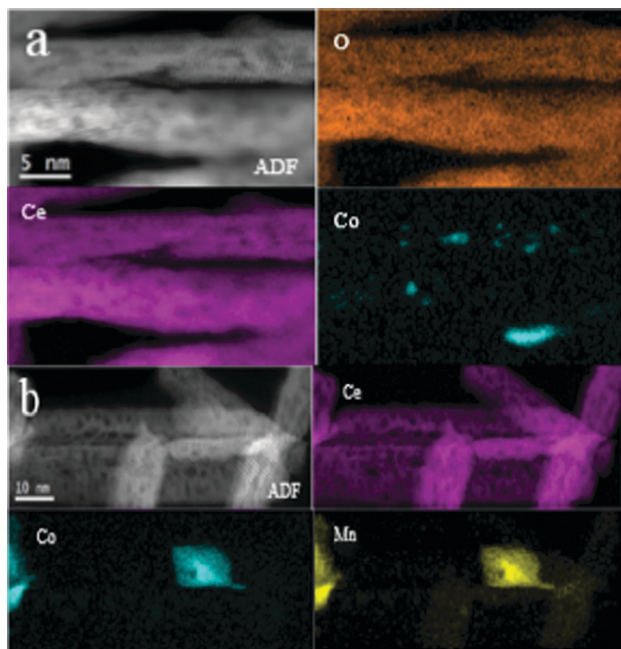
Fig. 5   Aberration-corrected HAADF-STEM with EELS results for fresh ceria-supported cobalt–manganese oxide samples: (a) CoO_x/CeO_2; (b) $CoMnO_x/CeO_2$.

cobalt–manganese oxides, instead of two isolated phases, were generated on the surface of ceria nanorods. Very recently, Grzybek *et al.* prepared Co_3O_4/CeO_2 catalysts by incipient wetness impregnation and also found the strong dispersion of cobalt oxide species ($\sim$10 nm in size) over the ceria support with the aid of HAADF-STEM images with EDX elemental mapping.[40] Furthermore, since the average width of ceria nanorods is *ca.* 8 nm (see Table 3), the 10 nm is only for length of bimetallic cobalt–manganese oxide particle, instead of its width or thickness.

Conventional characterization methods, such as XRD, normally show the average structural information of predominantly CeO_2 nanorods in our study. However, the local coordination structures around the Co active sites, which play crucial roles in the CO oxidation reaction, were unknown. Therefore, the XAFS technique, an elementally sensitive and extremely powerful tool to determine both electronic and local coordination structures, was used to investigate the ceria-supported bimetallic oxides. The X-ray absorption near edge spectroscopy (XANES) region in XAFS responds to the electronic structure of the tested cobalt atoms. The edge energy, the white line intensity and the pre-edge features are related to the oxidation state of $Co^{3+}/Co^{2+}/Co^0$. With the aid of cobalt standards (Co foil, CoO and Co_3O_4), the XANES profiles in Fig. 6a and b show that the Co_3O_4 composition was dominant for either fresh or used samples of both single metal oxide (CoO_x/CeO_2) and bimetallic oxides ($CoMnO_x/CeO_2$). Furthermore, linear combination analysis[41] was applied to determine the averaged oxidation state (δ) of cobalt to be 2.4 and 2.5 for fresh CoO_x/CeO_2 and $CoMnO_x/CeO_2$ (see Table 4), respectively, close to that for pure Co_3O_4 (8/3). After the CO oxidation reaction, the δ value of CoO_x/CeO_2 slightly decreased to 2.3, corresponding to the minor reduction of the cobalt species while the δ value of $CoMnO_x/CeO_2$ was maintained at 2.5.
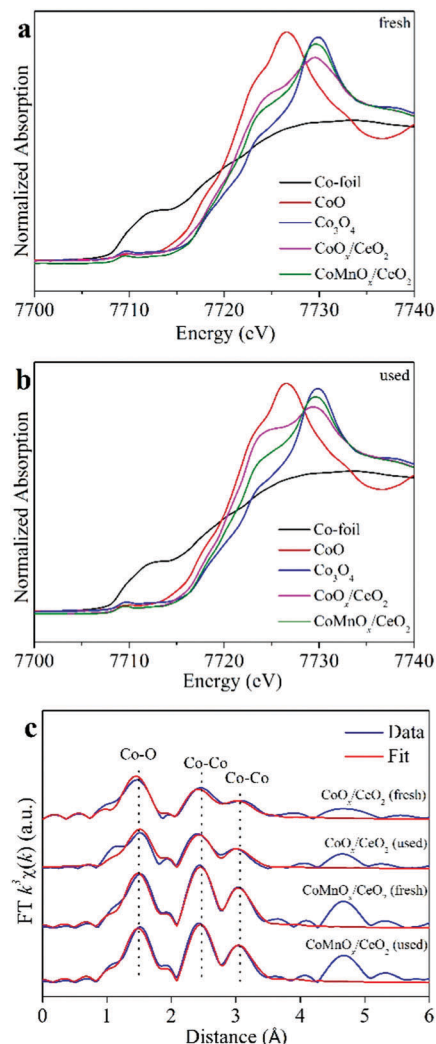
Fig. 6   Co K-edge XANES profiles (a and b) and EXAFS fitting results in R space (c) of ceria-supported cobalt–manganese oxide samples: (a and c) fresh; (b and c) used.

The extended X-ray absorption fine structure (EXAFS) part with the profile fitting was carried out to determine the short-range local structure including distances (R) and coordination number (CN) around the investigated cobalt atoms. Fig. 6c displays the EXAFS spectra in real space for fresh and used ceria-supported cobalt–manganese oxide samples, and the related fitting results are included in Table 4. Generally, the presented EXAFS spectra of all the measured catalysts exhibit a strong first shell of Co–O at 1.90–1.94 Å with a coordination number (CN) of 3.7–5.1, plus two second shells of Co–Co (R: 2.84–2.87 and 3.34–3.38 Å; CN: 2.5–4.9 and 2.7–5.6). These parameters are very similar to those of the pure Co_3O_4 model (see Table 4), indicating that the XRD-invisible cobalt oxide species should be the Co_3O_4 phase. Here, we need to mention that the contribution by Co–Co and Co–Mn bond pairs cannot be distinguished by the EXAFS fittings in $CoMnO_x/CeO_2$. So, we only used the Co–Co shell to describe the coordination structure of the secondary Co–M (M = Co or Mn) shell, since C_{Mn} is much lower than C_{Co} in this sample.

Table 4 Oxidation state of cobalt (δ) and Co K-edge EXAFS fitting results (R: distance; CN: coordination number; σ^2: Debye–Waller factor; ΔE_0: inner potential correction) of ceria-supported cobalt–manganese oxide samples

Sample	δ	Co–O R (Å)	Co–O CN	Co–Co R (Å)	Co–Co CN	σ^2 (Å²)	ΔE_0 (eV)
CoO$_x$/CeO$_2$ (fresh)	2.4	1.91 ± 0.01	4.0 ± 0.5	2.84 ± 0.02	2.5 ± 0.6	0.003 ± 0.001 (O)	3.6 ± 1.0
				3.34 ± 0.02	3.2 ± 1.0	0.005 ± 0.001 (Co)	
CoO$_x$/CeO$_2$ (used)	2.3	1.94 ± 0.01	3.7 ± 0.4	2.85 ± 0.01	2.6 ± 0.5		
				3.36 ± 0.02	2.7 ± 0.7		
CoMnO$_x$/CeO$_2$ (fresh)	2.5	1.93 ± 0.01	5.1 ± 0.3	2.87 ± 0.01	4.9 ± 0.4		4.1 ± 0.6
				3.38 ± 0.01	5.6 ± 0.6		
CoMnO$_x$/CeO$_2$ (used)	2.5	1.93 ± 0.01	5.0 ± 0.4	2.87 ± 0.01	4.6 ± 0.4		
				3.38 ± 0.01	5.2 ± 0.6		
CoMnO$_x$/CeO$_2$-1	2.5	1.91 ± 0.01	5.6 ± 0.3	2.85 ± 0.01	4.9 ± 0.4		4.1 ± 0.6
				3.36 ± 0.01	5.1 ± 0.6		
CoMnO$_x$/CeO$_2$-2	2.4	1.90 ± 0.01	4.6 ± 0.5	2.85 ± 0.01	3.2 ± 0.5		3.6 ± 1.0
				3.36 ± 0.01	2.9 ± 0.9		
Co	0	—	—	2.491	12		
Co$_3$O$_4$	8/3	1.943	6	2.874	6		
				3.370	6		
CoO	2	2.132	6	3.014	12		

We also observed that the fitted coordination parameters (R and CN of Co–O and Co–Co) of both bimetallic oxides and single metal oxide nanostructures are nearly identical before and after the catalytic tests (see Table 4). This confirms the good structural stability of ceria-supported cobalt–manganese oxide nanocatalysts for CO oxidation, which is in good agreement with the XRD and Raman results. Furthermore, we found that the CN values of Co–O and Co–Co shells for CoMnO$_x$/CeO$_2$ are distinctly larger than those for CoO$_x$/CeO$_2$ (see Table 4). This can be attributed to the higher crystallinity of the cobalt phase in ceria-supported bimetallic oxide nanocatalysts, revealing that the addition of manganese significantly enhanced the crystal growth of Co$_3$O$_4$ on the CeO$_2$ surface.

Therefore, on the basis of the above HAADF-STEM with EELS and XANES/EXAFS results, the cobalt oxide species supported on ceria nanorods have a Co$_3$O$_4$-type structure, which is strongly dispersed over the CeO$_2$ surface with sizes ranging from sub-nanometers to *ca.* 10 nm. Considering that these nanostructures were composed of 8.7 at% metals (Co or Co + Mn), but invisible in both XRD and TEM/HRTEM, we can draw the conclusion that these ~10 nm cobalt–manganese oxide species have two-dimensional dispersion over the ceria nanorods. Since the absorption energy of the Mn K edge (6539 eV) is severely overlapped with that of the Ce L1 edge (6548 eV), the corresponding XAFS spectra could not be collected and we utilized X-ray photoelectron spectroscopy (XPS) to determine the electronic structure of Ce, Mn and O for our ceria-supported cobalt–manganese oxide nanocatalysts.

Table 2 shows that the surface metal ratio of Mn/Ce is in the range of 6.9/93.1–8.5/91.5 for either fresh or used cobalt–manganese oxide nanocatalysts, which is distinctly larger than the bulk concentration of manganese ion in CoMnO$_x$/CeO$_2$ (3.0 at%) or MnO$_x$/CeO$_2$ (3.5 at%). This reveals that the Mn species enrich on the surface of ceria nanorods. Fig. 7a displays that the Ce 3d spectra of fresh and used samples are very similar, without significant changes of cerium oxidation state before and after the CO oxidation reaction. Fig. 7b shows two
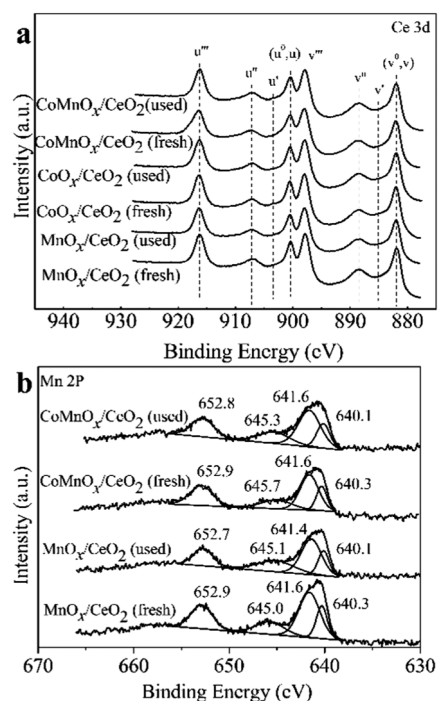
Fig. 7 XPS spectra of ceria-supported cobalt–manganese oxide samples: (a) Ce 3d; (b) Mn 2p.

major bands centered at 641.4–641.6 eV and 652.7–652.9 eV for Mn 2p$_{3/2}$ and for Mn 2p$_{1/2}$, respectively, either the single metal oxide (MnO$_x$/CeO$_2$) or the bimetallic oxide (CoMnO$_x$/CeO$_2$) sample. The peak deconvolution was performed on Mn 2p$_{3/2}$ spectra with the aim of determining the characteristic peaks of the Mn species, including Mn^{2+} (640.1–640.3 eV), Mn^{3+} (641.4–641.6 eV) and Mn^{4+} (645.0–645.7 eV).[42] Furthermore, Table 2 lists the surface component ratio of Mn^{2+}/Mn^{3+}/Mn^{4+}, which gives an averaged oxidation state equal to Mn(III) in each catalyst. This is reasonable if we consider the successful doping of Mn^{3+} ions into the Co$_3$O$_4$ matrix.

14538 | *Phys. Chem. Chem. Phys.*, 2017, **19**, 14533–14542

This journal is © the Owner Societies 2017
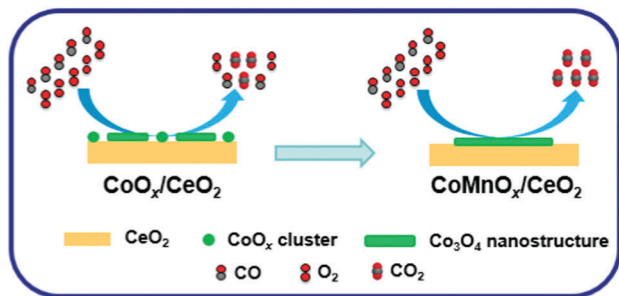
Scheme 1 Schematic demonstration of "structure–activity" relationship on ceria-supported cobalt–manganese oxide nanocatalysts.

However, creating and stabilizing more active cobalt species is still a very open discussion for us. In this work, we added manganese oxide into the ceria-supported cobalt oxide catalysts and found a significant enhancement of catalytic activity for the CO oxidation reaction. With the aid of multiple characterization approaches, we obtained the "structure–activity" relationship for the supported bimetallic cobalt–manganese oxide nanocatalyst, which has been demonstrated in Scheme 1.

Both ultra-fine cobalt oxide clusters (<2 nm) and Co_3O_4 nanostructures (~ 5 nm) form for CoO_x/CeO_2 if single metal (Co) ions are deposited onto the CeO_2 surface. This has been verified by the HAADF-STEM with EELS data (see Fig. 5a), as well as the EXAFS fitting results (see Fig. 6c). The CN values of Co–O and Co–Co are distinctly lower than the ideal Co_3O_4 model (see Table 4), which identifies the low crystallinity of Co_3O_4 in CoO_x/CeO_2. When the secondary phase of manganese oxide is introduced, the ceria-supported bimetallic metal oxide nanostructures ($CoMnO_x/CeO_2$) show better catalytic performance than the single metal (Co) oxide catalyst for the CO oxidation reaction (Fig. 1a). Here, the HAADF-STEM with EELS (see Fig. 5b) and EXAFS results (see Fig. 6c and Table 4) confirmed that the size of the cobalt oxide species increases from *ca.* 5 nm to *ca.* 10 nm, accompanied by the elimination of ultra-fine (<2 nm) cobalt oxide clusters. Thus, the key factor governing the CO oxidation reactivity should be related to the crystallinity of Co_3O_4 phase in supported cobalt oxide nanocatalysts. Previously, Grillo *et al.* proposed that the interaction between CO and Co^{3+} cations is fundamental for a significant CO oxidation capacity because the reduction of Co^{3+} to Co^{2+} allows harboring the excess electrons upon CO formation until being deoxidized by oxygen.[43] Jansson also claimed that CO is adsorbed on an oxidized cobalt site (probably Co^{3+}) and the adsorbed CO reacts with an oxygen linked to the active Co^{3+}.[44] Therefore, the stabilization of Co^{3+} species is important for the CO oxidation activity. In our work, the abundant Co^{3+} ions in the highly crystallized Co_3O_4 phase for $CoMnO_x/CeO_2$ could contribute to the higher reactivity than the single metal oxide counterpart (CoO_x/CeO_2).

To further investigate the contribution of manganese oxide to the crystal growth of the Co_3O_4 phase, we designed and completed the following experiments for catalyst preparation. The Co and Mn ions were sequentially deposited onto the CeO_2 surface, which is denoted as $CoMnO_x/CeO_2$-1 (Mn deposition → Co deposition)
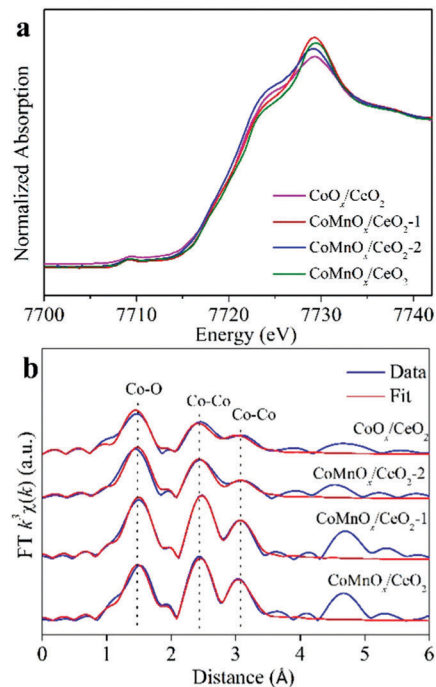
Fig. 8 Co K-edge XANES profiles (a) and EXAFS fitting results in *R* space (b) of fresh ceria-supported cobalt–manganese oxide samples with different deposition sequences.

and $CoMnO_x/CeO_2$-2 (Co deposition → Mn deposition). Fig. 8a depicts that the XANES profiles of as-calcined $CoMnO_x/CeO_2$-1 and $CoMnO_x/CeO_2$-2 are similar to that of Co_3O_4 and the averaged oxidation states are also close to 8/3 (see Table 4). However, as for the EXAFS fitting results, significant differences were observed between these two samples (see Fig. 8b), *i.e.* the coordination structure of cobalt in $CoMnO_x/CeO_2$-2 is more similar to that in CoO_x/CeO_2 (lower CN values of Co–O and Co–Co shells); while the coordination structure of cobalt in $CoMnO_x/CeO_2$-1 is nearly identical to that in $CoMnO_x/CeO_2$ (higher CN values of Co–O and Co–Co shells). Therefore, we can see that the initial presence of manganese oxide, either co-deposition with Co or before Co deposition, plays a crucial role in enhancing the crystallinity of Co_3O_4 during the synthesis of ceria-supported cobalt oxide nanocatalysts.

Conclusions

In this work, ceria nanorods were used as the support to anchor bimetallic cobalt–manganese oxide species *via* the deposition–precipitation approach. The main structure and texture of ceria nanorods are identical to those of pure CeO_2 support. With the aid of HAADF-STEM with EELS measurements, we identified that both ultra-fine clusters and ~ 5 nm nanocrystals are present for the single metal (Co) oxide sample while only enlarged nanostructures with *ca.* 10 nm in size are dominant for the bimetallic cobalt–manganese oxide catalyst. With the help of XANES analyses and the corresponding EXAFS fittings, we determined that the cobalt oxide nanostructures are of cubic Co_3O_4 phase, and the introduction of secondary manganese

oxide component improves the crystallization of surface two-dimensional cobalt oxide nanostructure over the ceria nanorods. The CO oxidation tests verified that bimetallic cobalt–manganese oxide catalyst is superior to the single metal (Co) oxide counterpart. Correlating with the catalytic performance, we drew a conclusion that the higher the crystallinity of metal oxide nanostructures, the higher the reactivity on ceria-supported cobalt-based catalysts for the low-temperature CO oxidation reaction.

Experimental

Materials

All the chemicals used in this work were of analytical grade and purchased from Sinopharm Chemical Reagent Co., Ltd without any further purification.

Synthesis

Preparation of ceria nanorods. The ceria nanorods were synthesized according to the hydrothermal method.[45] $Ce(NO_3)_3 \cdot 6H_2O$ (4.5 mmol) was added into an aqueous NaOH (6 M, 60 mL) solution under vigorous stirring. After the precipitation process was completed (about 10 min), the stock solution was transferred into a Teflon bottle, and further tightly sealed in a stainless-steel autoclave. The hydrothermal procedure was carried out in a temperature-controlled electric oven at 100 °C for 24 h. The precipitates were separated by centrifugation and then washed four times with deionized water and once with ethanol. The ceria support was obtained by drying the as-washed product in air under 70 °C overnight.

Deposition of cobalt–manganese oxide clusters. Ceria-supported cobalt–manganese oxide clusters samples were synthesized via a deposition–precipitation method.[46] $Mn(NO_3)_2 \cdot 4H_2O$ (0.3 mmol), $Co(NO_3)_2 \cdot 6H_2O$ (0.6 mmol) and the as-calcined CeO_2 nanorods (1 g) were suspended in 100 mL Millipore (>18 MΩ) water under vigorous stirring. Then, Na_2CO_3 aqueous solution (0.5 M) was dropped into the above solution until a final pH value of ~9 was reached. After the generation of greenish slurries, the stock solution was further aged at room temperature for another 2 h. The as-obtained precipitates were filtered and then washed by Millipore water three times. The as-washed powders were dried in a vacuum at 80 °C overnight and then calcined in still air at 400 °C for 4 h (ramping rate: 2 °C min⁻¹). The ceria-supported bimetallic cobalt–manganese oxide was denoted as $CoMnO_x/CeO_2$, and the single metal oxide samples of pure cobalt or manganese were labeled as CoO_x/CeO_2 or MnO_x/CeO_2, respectively. For comparison, we also resorted to a two-step sequential deposition–precipitation approach to prepare cobalt–manganese oxide. Cobalt oxide was introduced into the as-calcined ceria-supported manganese oxide to form $CoMnO_x/CeO_2$-1; while manganese oxide was added into the as-calcined ceria-supported cobalt oxide to generate $CoMnO_x/CeO_2$-2.

Characterizations

The metal ratios of Co/Mn/Ce were determined by inductively coupled plasma atomic emission spectroscopy (ICP-AES) on an IRIS Intrepid II XSP instrument (Thermo Electron Corporation).

The nitrogen adsorption–desorption measurements were performed on an ASAP2020-HD88 analyzer (Micromeritics Co. Ltd) at 77 K. The measured powders were degassed at 250 °C under vacuum (<100 μm Hg) for over 4 h. The BET specific surface areas (S_{BET}) were calculated from data in the relative pressure range between 0.05 and 0.20.

The powder X-ray diffraction (XRD) patterns were recorded on a Bruker D8 Advance diffractometer (40 kV, 40 mA) with a scanning rate of 4° min⁻¹, using Cu $K_{\alpha 1}$ radiation (λ = 1.5406 Å). The diffraction patterns were collected from 20 to 80° with a step of 0.02°. The 2θ angles were calibrated with a μm-scale alumina disc. The powder sample after grinding was placed inside a quartz sample holder for each test. With the software "LAPOD" of least-squares refinement of cell dimensions of cubic CeO_2 from powder data by Cohen's method.[47,48]

Raman spectra were acquired by excitation of the sample at 532 nm using a Raman microscope system (HORIBA JOBIN YVON) in the spectral window from 100 to 800 cm⁻¹ with a spectral resolution of 2 cm⁻¹.

The transmission electron microscopy (TEM) and high-resolution TEM (HRTEM) images were collected on a FEI Tecnai F20 microscope operating at 200 kV. The aberration-corrected high-angle annular dark-field scanning transmission electron microscopy (HAADF-STEM) images and electron energy-loss spectroscopy (EELS) measurements were performed on a JEOL ARM200F microscope equipped with a probe-forming spherical-aberration corrector and a Gatan image filter (Quantum 965). Elemental mapping results were obtained from the Co-$L_{2,3}$, Mn-$L_{2,3}$, Ce-$M_{4,5}$ and O-K edges in the EELS spectra.

The X-ray photoelectron spectroscopy (XPS) analysis was performed on an Axis Ultra XPS spectrometer (Kratos, UK) with 225 W of Al Kα radiation. The C 1s line at 284.8 eV was used to calibrate the binding energies.

X-ray absorption fine structure

The X-ray absorption fine structure (XAFS) spectra at Co K (E_0 = 7709 eV) edge were obtained at BL14W1 beamline[49] of Shanghai Synchrotron Radiation Facility (SSRF) operated at 3.5 GeV under "top-up" mode with a constant current of 220 mA. The XAFS data were recorded in fluorescence mode with a standard Lytle ion chamber. The energy was calibrated according to the absorption edge of pure Co foil.

Athena and Artemis codes were used to extract the data and fit the profiles. For the X-ray absorption near edge structure (XANES) part, the experimental absorption coefficients as functions of energies $\mu(E)$ were processed by background subtraction and normalization procedures, and reported as "normalized absorption". Based on the normalized XANES profiles, the chemical valence of cobalt was determined by linear combination analysis[41] with the references of Co/CoO/Co_3O_4.

For the extended X-ray absorption fine structure (EXAFS) part, the Fourier transformed (FT) data in R space were analyzed by applying Co_3O_4 model for Co–O and Co–Co contributions. The passive electron factor, S_0^2, was determined by fitting the experimental data on the Co foil and fixing the coordination number (CN) of Co–Co to be 12, and then fixed for further

analysis of the measured samples. The parameters describing the electronic properties (*e.g.*, correction to the photoelectron energy origin, E_0) and local structure environment including CN, bond distance (R) and Debye–Waller (D.W.) factor around the absorbing atoms were allowed to vary during the fitting process. The fitted ranges for k and R spaces were selected to be $k = 3$–12 Å^{-1} with $R = 1$–4 Å (k^3 weighted).

Catalytic tests

The temperature-programmed reduction by hydrogen (H_2-TPR) was conducted in a Builder PCSA-1000 instrument equipped with a thermal conductivity detector (TCD). The reduction process was carried out in a mixture of 5% H_2/Ar (30 mL min^{-1}) from room temperature to 600 °C (5 °C min^{-1}). The sieved catalysts (40–60 mesh, 30 mg) were pretreated in pure O_2 at 300 °C for 30 min before each test.

The CO oxidation activities for ceria-supported cobalt–manganese oxide samples were evaluated at 30 °C. The outlet gas compositions of CO and CO_2 were monitored online by a non-dispersive IR spectroscopy (Gasboard 3500, Wuhan Sifang Company, China). The CO conversion was calculated according to the following equations: CO conversion (%) = ($CO_{in} - CO_{out}$)/$CO_{in} \times 100$. The reaction rates were calculated within the range of 3–20% CO conversion.

Notes and references

1 M. Haruta, N. Yamada, T. Kobayashi and S. Iijima, *J. Catal.*, 1989, **115**, 301–309.

2 M. Date, M. Okumura, S. Tsubota and M. Haruta, *Angew. Chem., Int. Ed.*, 2004, **43**, 2129–2132.

3 Y. Yu, T. Takei, H. Ohashi, H. He, X. Zhang and M. Haruta, *J. Catal.*, 2009, **267**, 121–128.

4 K. Ramesh, L. Chen, F. Chen, Y. Liu, Z. Wang and Y. F. Han, *Catal. Today*, 2008, **131**, 477–482.

5 L. H. Hu, Q. Peng and Y. D. Li, *J. Am. Chem. Soc.*, 2008, **130**, 16136–16137.

6 X. W. Xie, Y. Li, Z. Q. Liu, M. Haruta and W. J. Shen, *Nature*, 2009, **458**, 746–749.

7 D. A. H. Cunningham, T. Kobayashi, N. Kamijo and M. Haruta, *Catal. Lett.*, 1994, **25**, 257–264.

8 C. X. Liu, Q. Liu, L. Bai, A. Q. Dong, G. B. Liu and S. H. Wen, *J. Mol. Catal. A: Chem.*, 2013, **370**, 1–6.

9 L. H. Hu, K. Sun, Q. Peng, B. Xu and Y. Li, *Nano Res.*, 2010, **3**, 363–368.

10 J. Jansson, A. E. C. Palmqvist, E. Fridell, M. Skoglundh, L. Österlund, P. Thormählen and V. Langer, *J. Catal.*, 2002, **211**, 387–397.

11 X. Wang, W. Zhong and Y. W. Li, *Catal. Sci. Technol.*, 2015, **5**, 1014–1020.

12 S. C. Petitto, E. M. Marsh, G. A. Carson and M. A. C. Langell, *J. Mol. Catal. A: Chem.*, 2008, **281**, 49–58.

13 M. J. Pollard, B. A. Weinstock, T. E. Bitterwolf, P. R. Griffiths, A. P. Newbery and J. B. Paine III, *J. Catal.*, 2008, **254**, 218–225.

14 J. Li, G. Z. Lu, G. S. Wu, D. S. Mao, Y. L. Guo, Y. Q. Wang and Y. Guo, *Catal. Sci. Technol.*, 2014, **4**, 1268–1275.

15 J. Zheng, W. Chu, H. Zhang, C. F. Jiang and X. Y. Dai, *J. Nat. Gas Chem.*, 2010, **19**, 583–588.

16 Y. F. Su, Z. C. Tang, W. L. Han, Y. Song and G. X. Lu, *Catal. Surv. Asia*, 2015, **19**, 68–77.

17 J. Li, G. Z. Lu, G. S. Wu, D. S. Mao, Y. Q. Wang and Y. Guo, *Catal. Sci. Technol.*, 2012, **2**, 1865–1871.

18 F. Grillo, M. M. Natile and A. Glisenti, *Appl. Catal., B*, 2004, **48**, 267–274.

19 C. H. Kuo, W. K. Li, W. Q. Song, Z. Luo, A. S. Poyraz, Y. Guo, A. W. K. Ma, S. L. Suib and J. He, *ACS Appl. Mater. Interfaces*, 2014, **6**, 11311–11317.

20 J. Y. Luo, M. Meng, Y. Q. Zha and L. H. Guo, *J. Phys. Chem. C*, 2008, **112**, 8694–8701.

21 D. Y. Deng, N. Chen, Y. X. Li, X. X. Xing and X. C. Xiao, *Catal. Lett.*, 2015, **145**, 1344–1350.

22 K. Rida, A. L. Camara, M. A. Pena, C. L. B. Diaz and A. M. Arias, *Int. J. Hydrogen Energy*, 2015, **40**, 11267–11278.

23 Z. G. Liu, S. H. Chai, A. Binder, Y. Y. Li, L. T. Ji and S. Dai, *Appl. Catal., A*, 2013, **451**, 282–288.

24 J. Y. Luo, M. Meng, X. Li, X. G. Li, Y. Q. Zha, T. D. Hu, Y. N. Xie and J. Zhang, *J. Catal.*, 2008, **254**, 310–324.

25 N. J. Divins, A. Casanovas, W. Xu, S. D. Senanayake, D. Wiater, A. Trovarelli and J. Llorca, *Catal. Today*, 2015, **253**, 99–105.

26 J. Kugai, J. T. Miller, N. Guo and C. S. Song, *J. Catal.*, 2011, **277**, 46–53.

27 C. M. Olmos, L. E. Chinchilla, A. Villa, J. J. Delgado, H. Y. Pan, A. B. Hungria, G. Blanco, J. J. Calvino, L. Prati and X. W. Chen, *Appl. Catal., A*, 2016, **525**, 145–157.

28 E. B. Fox, S. Velu, M. H. Engelhard, Y. H. Chin, J. T. Miller, J. Kropf and C. S. Song, *J. Catal.*, 2008, **260**, 358–370.

29 L. W. Guo, P. P. Du, X. P. Fu, C. Ma, J. Zeng, R. Si, Y. Y. Huang, C. J. Jia, Y. W. Zhang and C. H. Yan, *Nat. Commun.*, 2016, **7**, 13481.

30 S. A. Mock, S. E. Sharp, T. R. Stoner, M. J. Radetic, E. T. Zell and R. G. Wang, *J. Colloid Interface Sci.*, 2016, **466**, 261–267.

31 T. Cwele, N. Mahadevaiah, S. Singh and H. B. Friedrich, *Appl. Catal., A*, 2016, **182**, 1–14.

32 D. Delimaris and T. Ioannides, *Appl. Catal., B*, 2008, **84**, 303–312.

33 L. Spadaro, F. Arena, M. L. Granados, M. Ojeda, J. L. G. Fierro and F. Frusteri, *J. Catal.*, 2005, **234**, 451–462.

34 N. K. Gamboa-Rosales, J. L. Ayastuy, M. P. Gonzalez-Marcos and M. A. Gutierrez-Ortiz, *Int. J. Hydrogen Energy*, 2012, **37**, 7005–7016.

35 W. W. Wang, P. P. Du, S. H. Zou, H. Y. He, R. X. Wang, Z. Jin, S. Shi, Y. Y. Huang, R. Si, Q. S. Song, C. J. Jia and C. Y. Yan, *ACS Catal.*, 2015, **5**, 2088–2099.

36 W. H. Weber, K. C. Hass and J. R. McBride, *Phys. Rev. B: Condens. Matter Mater. Phys.*, 1993, **48**, 178–185.

37 Y. J. Lee, G. H. He, A. J. Akey, R. Si, M. Flyzani-Stephanopoulos and I. P. Herman, *J. Am. Chem. Soc.*, 2011, **133**, 12952–12955.

38 R. Si and M. Flytzani-Stephanopoulos, *Angew. Chem., Int. Ed.*, 2008, **47**, 2884–2887.

39 B. Y. Lin, Y. C. Qi, K. M. Wei and J. X. Lin, *RSC Adv.*, 2014, **4**, 38093–38102.

40 G. Grzybek, P. Stelmachowski, S. Gudyka, P. Indyka, Z. Sojka, N. Guillen-Hurtado, V. Rico-perez, A. Bueno-Lopez and A. Kotarba, *Appl. Catal., B*, 2016, **180**, 622–629.

41 A. I. Frenkel, Q. Wang, N. Marinkovic, J. G. Chen, L. Barrio, R. Si, A. L. Cámara, A. M. Estrella, J. A. Rodriguez and J. C. Hanson, *J. Phys. Chem. C*, 2011, **115**, 17884–17890.

42 G. Liu, J. H. Liu, W. X. Li, C. Liu, F. Wang, J. K. He, C. Guild, H. Jin, D. Kriz, R. Miao and S. L. Suib, *Appl. Catal., A*, 2017, **535**, 77–84.

43 F. Grillo, M. M. Natile and A. Glisenti, *Appl. Catal., B*, 2004, **48**, 267–274.

44 J. Jansson, *J. Catal.*, 2000, **194**, 55–60.

45 H. X. Mai, L. D. Sun, Y. W. Zhang, R. Si, W. Feng, H. P. Zhang, H. C. Liu and C. H. Yan, *J. Phys. Chem. B*, 2005, **109**, 24380–24385.

46 P. P. Du, X. C. Hu, X. Wang, C. Ma, M. Du, J. Zeng, C. J. Jia, Y. Y. Huang and R. Si, *Inorg. Chem. Front.*, 2017, **4**, 668–674.

47 J. I. Langford, *J. Appl. Crystallogr.*, 1971, **4**, 259–260.

48 J. I. Langford, *J. Appl. Crystallogr.*, 1973, **6**, 190–196.

49 H. S. Yu, X. J. Wei, J. Li, S. Q. Gu, S. Zhang, L. H. Wang, J. Y. Ma, L. N. Li, Q. Gao, R. Si, F. F. Sun, Y. Wang, F. Song, H. J. Xu, X. H. Yu, Y. Zou, J. Q. Wang, Z. Jiang and Y. Y. Huang, *Nucl. Sci. Tech.*, 2015, **26**, 050102.